Grounding-zone flow variability of Priestley Glacier, Antarctica, in a diurnal tidal regime

R. Drews[1], C. T. Wild[2,3], O. J. Marsh[4], W. Rack[3], T. A. Ehlers[1], N. Neckel[5], V. Helm[5]

[1]Department of Geosciences, Tbingen University, Germany
[2]College of Earth, Ocean, and Atmospheric Sciences, Oregon State University, Oregon, USA
[3]Gateway Antarctica, Canterbury University, Christchurch, New Zealand
[4]British Antarctic Survey, Cambridge, UK
[5]Alfred Wegener Institute, Helmholtz Centre for Polar- and Marine Research, Bremerhaven, Germany

Key Points:

- Terrestrial radar interferometry at Priestley Glacier, Antarctica, quantifies sub-daily ice-stream velocity changes due to ocean tides.
- Ice-flow is fastest with falling tide and slowest with rising tide. Tidal modulation decays linearly over 10 km upstream from the grounding line.
- Tidal flexure is detected hourly, including cm vertical uplift upstream of the grounding line. This constrains grounding-zone processes.

Corresponding author: Reinhard Drews, `reinhard.drews@uni-tuebigen.de`

Abstract

Dynamics of polar outlet glaciers vary with ocean tides, providing a natural laboratory to understand basal processes and ice rheology. We apply Terrestrial Radar Interferometry to close the spatiotemporal gap between GNSS and satellite observations. Three-hour flowfields collected over an eight day period at Priestley Glacier, Antarctica, validate and provide the spatial context for concurrent GNSS measurements. Ice flow is fastest during falling tides and slowest during rising tides. Principal components of the time-series prove upstream propagation of tidal signatures > 10 km away from the grounding line. Hourly, cm-scale horizontal and vertical flexure patterns occur >6 km upstream of the grounding line. Vertical uplift upstream of the grounding line is consistent with ephemeral re-grounding during low-tide impacting grounding-zone stability. Taken together, these observations identify tidal imprints on ice-stream dynamics on new temporal and spatial scales providing constraints for models designed to isolate dominating processes in ice-stream mechanics.

Plain Language Summary

Temperatures in Antarcticas interior are virtually always below the freezing point, so that ice continuously accumulates through snowfall. This mass gain is balanced by ice transport from the interior towards the coast. There, ice is eventually attributed to the ocean through iceberg calving and ocean induced melting. Small changes in any of these processes impact on global ocean circulation and mean sea level. Most of the ice is transported by fast flowing ice streams. Interestingly, the speed of the ice streams at Antarctica's boundaries varies with ocean tides, but we don't know why. We use a specialized instrument, that measures the speed of the ice area-wide every few hours. We observe velocity fluctuations and flexing of the ice over tidal cycles. This will help us to understand how the tidal signal propagates into ice-streams, and eventually teach us what the underlying processes of ice-stream formation are.

1 Introduction

The mass budget of Antarctica is controlled by a network of ice streams draining from the Antarctic plateau towards the ocean. At the grounding line, ice starts to float forming ice shelves where ice is attributed to the ocean through basal melting and iceberg calving. Ice-stream dynamics are modulated by ocean tides (Rosier et al., 2017) providing a rigorous test case for processes controlling ice discharge (Padman et al., 2018). Relevant processes include elastic and viscous stress transmission across the grounding line (Thompson et al., 2014), changing subglacial hydrology (Rosier & Gudmundsson, 2016), changing ice-shelf buttressing (Rosier & Gudmundsson, 2018), temporal ungrounding (Minchew et al., 2017), as well as imprints in sediment flow and till strength (Walker et al., 2013; Christianson et al., 2013). All of these processes are poorly constrained by observations, yet important for model projections of Antarctic ice discharge.

Tides influence both the horizontal and vertical components of ice-stream dynamics. Horizontal flow is modulated most strongly on fortnightly spring-to-neap tidal frequencies (Gudmundsson, 2006). Diurnal and semi-diurnal modulations are an order of magnitude smaller, suggesting that ice streams respond non-linearly to peak-to-peak changes in tidal amplitudes. Much progress in understanding this behavior has resulted in sophisticated models using 3D geometries and a viscoelastic rheology (Thompson et al., 2014; Rosier et al., 2015). However, there are significant differences in how tidal forces are coupled to ice-sheet models (Rosier & Gudmundsson, 2016), and all of them require a high degree of tuning to match the contrasting behavior of different ice streams around Antarctica. For glaciers feeding into the Ronne Ice Shelf, tidal signatures persist more than 80 km upstream of the grounding line (Rosier et al., 2017). In areas with smaller tidal amplitudes, tidal signatures are not seen at all (Scott et al., 2009) or up to only a

few kilometers upstream of the grounding line (Riedel et al., 1999; Heinert & Riedel, 2007). The controls behind this large spread in observations are unknown (Padman et al., 2018). Vertical deflection by tides may impact grounding-zone morphology through flexural bulging. This occurs if a hypothesized fulcrum at the grounding line leverages vertical deflection upstream of the grounding line (Walker et al., 2013). If true, this deflection pumps ocean water upstream of the grounding line changing basal melting and till properties, which consequently impacts grounding-line stability (Christianson et al., 2013).

Horizontal flow variability on tidal timescales is detectable in high-fidelity GNSS time series. However, these point-measurements do not provide the required spatial context (Thompson et al., 2014). Only a few ground-based observations (Smith, 1991; Heinert & Riedel, 2007) provide direct observational support for vertical uplift upstream of the grounding line. Whether this is because most receivers are located outside of the uplift zone, or because uplift is absent or too small to be measured is unclear. Satellites, on the other hand, provide excellent spatial coverage but with orbital repeat intervals linked to an integer number of days, they alias the tidal cycle and are therefore also problematic for investigating tidal effects. Even for cases of exceptional temporal coverage, satellite-derived measurements need to be synthesized over multiple tidal cycles and require a-priori assumptions of sinusoidal dynamics (Minchew et al., 2017). Furthemore, vertical deflection upstream of the grounding line has not been confirmed by satellites, mostly due to challenges in disentangling tidal induced horizontal from vertical motion when using interferometric SAR (Rack et al., 2017; Wild et al., 2019). The lack of spatially coherent flow fields on sub-daily timescales is thus a bottleneck for understanding processes controlling ice-stream modulation by ocean tides.

Here, we close the gap between localized GNSS observations and satellite coverage using Terrestrial Radar Interferometry (TRI) (Caduff et al., 2015). TRI has been applied previously in Greenland (Voytenko et al., 2017; Xie et al., 2018), but not in Antarctica where logistical constraints are larger. We successfully surveyed the grounding zone of Priestley Glacier, a deeply incised valley glacier draining ice from the Antarctic Plateau through the Transantarctic Mountains into the Nansen Ice Shelf. Near the zone where tidal flexure occurs, surface velocities average $\sim$160 ma^{-1}, ice thickness is $\sim$1200 m, and the ice-bed interface is $>$ 500 m below sea level for $>$ 80 km inland. Tides are predominantly diurnal (at S_1, K_1 frequencies) with amplitudes of $\pm$0.4 m. Priestley Glacier provides a unique opportunity to study the upstream signal propagation of ocean tides, because an ice-free ridge elevated 1000 m above the glacier surface provides a firm anchor and a good viewpoint for TRI across the grounding zone (Fig. 1a).

2 Methods

2.1 Derivation of line-of-sight velocities and grounding zone flexure using Terrestrial Radar Interferometry

TRI data were acquired using a Gamma Remote Sensing Portable Radar Interferometer (GPRI-2) with a maximum range of 16 km, assembling coherent images line-by-line while being rotated by 180° (Caduff et al., 2015). Images were acquired at 3 min intervals and gridded to 10 m postings. Ice speed was mapped in a moving average every 0.5 h in a line-of-sight (LOS) geometry using standard satellite interferometry techniques (Rosen et al., 2000). Each LOS velocity field results from multi-temporal stacking of $\sim$50 unwrapped interferograms with a minimum temporal baseline of 2.8 h in a 3 h time period. Stacking reduces atmospheric noise and results in residual random velocities at the ice-free rock walls within the scene, typically $<$ 10% of the glacier velocities. Images were georeferenced by matching observed and synthetic scenes based on the REMA elevation model (Howat et al., 2019) using the radar look vector as a tuning variable.

The LOS velocity could be mapped to a 3D flowfield, were the flow direction known a priori (Voytenko et al., 2015). Here, we cannot rule out the flow direction varying over tidal timescales and so the GNSS measurements are projected into LOS of the TRI. The projection between TRI LOS velocity ($v_{LOS} > 0$ for movement towards the sensor) and the 3D GNSS glacier velocity $v = (v_x, v_y, v_z)$ referenced in polar stereographic coordinates is given by

$$v_{LOS}(t_1,t_2) = \underbrace{\sin(\phi)\cos(\theta)}_{s_x}\overbrace{v_x(t_1,t_2)}^{\frac{x_2-x_1}{t_2-t_1}} + \underbrace{\sin(\phi)\sin(\theta)}_{s_y}\overbrace{v_y(t_1,t_2)}^{\frac{y_2-y_1}{t_2-t_1}} + \underbrace{\cos(\theta)}_{s_z}\overbrace{v_z(t_1,t_2)}^{\frac{z_2-z_1}{t_2-t_1}} \quad (1)$$

where ϕ and θ are the azimuthal orientation and local incidence angles, respectively. This results in differing sensitivities (s_x, s_y, s_z) of TRI to horizontal and vertical velocities. For our geometry, the sensitivity is lowest for v_z and varies for v_x (approx. across-flow) and v_y (approx. along-flow) across the scene (Supplementary Information 1).

Tidal flexure and velocity variability were quantified by differencing individual interferograms with a common temporal baseline Δt formed out of image triplets collected at times t_1, t_2, and t_3:

$$v_{LOS}(t_1,t_2) - v_{LOS}(t_2,t_3) = \frac{1}{\Delta t}\left(\underbrace{s_x(2x_2 - x_1 - x_3)}_{d^2x} + \underbrace{s_y(2y_2 - y_1 - y_3)}_{d^2y} + \underbrace{s_z(2z_2 - z_1 - z_3)}_{d^2z}\right) \quad (2)$$

Differencing interferograms cancels the mean glacier flow and highlights effects of tidal flexure and tidal velocity change which are different between the three acquisitions (Rignot, 1996). The dense spacing of TRI acquisition enables differential interferometry with triplets of variable Δt and at 3 minute intervals. This is in stark contrast to satellites, which have repeat times of at least several days and hence alias tidal cycles. Because of the diurnal tides in our area of interest, flow variability is also largely diurnal and our results are shown at $\Delta t = 12$ h to maximize the signal.

2.2 Detecting flow variability with GNSS

GNSS data were collected with geodetic L1L2 receivers (hereafter referred to as Tuati, Blake, and Hillary) located along a center flowline across the grounding zone (Fig. 1b). Positions were computed every 15 s using Precise Point Positioning (PPP) and differential processing (D-GNSS) relative to a fixed basestation located at the TRI (Supplementary Information 2). Vertical and horizontal velocities were obtained from the slope of a linear regression over a minimum of 6 h corresponding to a maximum horizontal displacement of << 10 cm. For smaller time intervals, the velocity solutions from the different processing schemes diverge, with the D-GNSS solutions showing a less noisy signal. For the 12 h time differences applied in the differential interferometry, both D-GNSS and PPP are at the detection limit as the predicted differential vertical displacement is within centimeters.

2.3 Principal Component Analysis for the time series

To isolate the underlying spatial and temporal patterns in the TRI data set, principal component analysis is applied to the demeaned time series of N=288 TRI LOS velocity fields, each of them gridded to a raster with dimensions $n \times m$. This results in a decomposition of the TRI LOS velocity field $\mathbf{V}^i_{LOS}$ at time $i = 1..N$, into a new set

of $n \times m$ basis fields termed principal components ($\mathbf{PC}_j, j = 1..N$):

$$\mathbf{V}^i_{LOS} = \overline{\mathbf{V}}_{LOS} + \sum_{j=1}^{N} a^i_j \mathbf{PC}_j. \tag{3}$$

Here, $\overline{\mathbf{V}}_{LOS}$ is the temporally averaged TRI LOS velocity field and a^i_j represents the weights of $\mathbf{PC}_j$ for reconstructing the flowfield at time i. The a^i_j are normalized relative to $max(a^i_1)$ so that they range between -1 and 1. Elsewhere the principal components are also referred to as Empirical Orthogonal Functions (Campbell et al., 2017). They are orthogonal and sorted so that the explained variance decreases with increasing j. Reconstruction of $\mathbf{V}^i_{LOS}$ using eq. (3) is exact. However, in our case the first three $\mathbf{PC}_{1,2,3}$ explain 85% (=65% (PC1) + 13% (PC2) +7% (PC3)) of the total variance in our dataset. Moreover, as will be shown below, $\mathbf{PC}_{1,2,3}$ have a spatial pattern that can be meaningfully interpreted. $\mathbf{PC}_{j>5}$, on the other hand, contain signatures of atmospheric noise that are observed in single 3 min interferograms. The implications are twofold: (1) reconstruction of $\mathbf{V}^i_{LOS}$ with $j < 5$ is an efficient noise filter, and (2) time series analysis of $a^i_{1,2,3}$ determines the relevant frequencies for $\mathbf{PC}_{1,2,3}$ and thus provides the spatiotemporal context of tidal signal propagation upstream of the grounding line. The frequency spectrum of $a^i_{1,2,3}$ is calculated using a Fast Fourier Transform with a Hanning window to taper spurious frequencies caused by the finite length of the time series.

2.4 Detecting the extent of the grounding zone

For delineating areas in the grounding zone, we use terminology from satellite observations (Fricker et al., 2009; Rignot et al., 2011) defining the extent of the grounding zone as a function of vertical displacement due to ocean tides. The seaward limit of the grounding zone (point H) occurs where the ice shelf floats freely. The landward limit occurs where vertical displacement ceases (point F). This is typically upstream of the grounding line (point G). We locate G in an ice-penetrating radar transect from 2013 (Paden et al., 2010) using an abrupt change in basal reflectivity (Supplementary Information Fig S8). H is approximated using standard satellite interferometry mapping techniques (Rignot et al., 2011) to a set of 30 differential Sentinel 1A interferograms. These cover the time period from 2017 to 2019. The grounding zone is also mapped from a triplet of TanDEM-X aquisitions taken concurrent to our observations in November 2018 (Supplementary Information S7). In this context, the GNSS station Tuati is located at the grounding line approximately 1 km downstream of F. Blake is at or slightly upstream of F on grounded ice. Hillary is upstream of F (Fig. 1).

3 Results

3.1 Temporally persistent LOS flowfield patterns

The mean LOS velocity field (Fig. 1b) captures the ice-stream dynamics in several ways. First, the North-South directed ice flow is represented in the LOS velocity field with positive values (i.e., movement towards the sensor) on the upstream side and with negative values (i.e., movement away from the sensors) at the downstream side. Second, sensitivity is lowest to the along-flow direction in the scene center, explaining the comparatively low LOS velocity values there. Third, the three tributary glaciers flowing into the Priestley from the South (TG1-TG3) are all reliably detected. The ice-free rock walls show negligible velocity signals. Fourth, in the upstream section the LOS velocity exhibits an oscillation (marked in Fig. 1b and Fig. S8). This occurs in an area where closed phase contours appear in the corresponding interferograms, and is termed a *Bull's eye*. These kinds of patterns have been explained previously by ice flow over dynamically supported surface depressions (Joughin et al., 1995). This also applies here as the pattern is temporally persistent and occurs in an area of changing surface slope caused by ice

flow over a basal obstacle (Supplementary Fig. S8). This results in lowering and then in re-emergence of the ice-flow vector that is readily detected by the TRI.

3.2 Temporally variable flowfield patterns

At the grounding line (i.e., at Tuati), vertical velocities are highest at rising tides and lowest at falling tides. In contrast, horizontal velocities are slowest ($\sim$80 m a^1) during rising tides and fastest ($\sim$175 m a^1) during falling tides (Fig. 2a-c). This fixed phase relationship between tides and velocities has been observed previously (Marsh et al., 2013) and consistent with elastic stress transfer through vertical tidal displacement (Rosier et al., 2015). After projecting GNSS velocities into the TRI reference frame, both types of measurements differ by 3 ± 15 m a^{-1} in mean and standard deviation (Fig. 2d). This deviation is much smaller than the observed LOS velocity variability bracketing 30–110 m a^{-1}. Further upstream, the displacement in the 6 h solutions at GNSS stations Blake and Hillary is too small (< 10 cm) to show a meaningful velocity variability on tidal time scales. Daily averaged solutions agree with the TRI LOS velocities (-1 ± 6 m a^{-1}).

The LOS flowfield time series shows temporal variability that decreases near-linearly in the upstream direction with distance from the grounding line (Fig. 1c). At, and seawards, of the grounding line fluctuations are >50% relative to the mean, reflecting the vertical displacement by tides and changes in horizontal flow. Given our low sensitivity to vertical velocities, variability upstream of the grounding line predominantly reflects changes in horizontal flow.

The principal component analysis of the LOS flowfield time series (Fig. 3a) delivers important insights about the spatiotemporal signature of tidal ice-flow modulation at and upstream of the grounding line. First, the power spectrum of a_1, a_2 and a_3 peaks at the diurnal frequencies of the tidal forcing (Fig. 3b). Moreover, a_1 has its extremal values close to the rising and falling tides (Supplementary Figure 4). **PC1** exhibits a near-linear ramp decaying in magnitude with increasing distance from the grounding line, similar to the decaying variability in Fig. 1c. We interpret **PC1** as a spatial representation of how far and how strong the tidal forcing propagates upstream and modulate horizontal ice flow there. Second, a_2 and a_3 show extremal values during the rising and falling tides, but with opposite signs as a_1. Moreover, **PC2** and **PC3** have patterns of changing polarity. The zero crossing in **PC2** is close to the hinge line inferred in section 2.4. The combination of **PC2** and **PC3** approximate the tidal flexure zone detailed below. We, therefore, interpret **PC2** and **PC3** as signals of tidal modulation for the vertical velocities on the ice shelf, and also for tidal flexure further upstream. The principal components and their temporal variability provide the context for ice-flow modulation on diurnal timescales. This signal can only partially be recovered with the GNSS receivers upstream of the grounding line, suggesting that the TRI may have a higher sensitivity (at the cost of a 1D ice-flow representation) in this area.

3.3 Tidal flexure patterns

Tidal flexure patterns are quantified using differential displacements in GNSS and TRI over $\Delta t = 12$ h (eq. 2). This time-interval corresponds to the time difference between low-tide and high-tide in a diurnal tidal regime such as the Ross Sea, maximizing the tidal imprints in both datasets. In the GNSS data at Tuati (Fig. S3), the relationship of high horizontal velocities during falling tide and low horizontal velocities during rising tides is clearly evident in the detrended positions. This relationship is weaker, but still significant further upstream on grounded ice (i.e., at Blake (Fig. S4)). Even further upstream (i.e., at Hillary (Fig. S5)) no meaningful tidal signatures are detected with GNSS. Interestingly, while vertical deflection at Tuati is synchronous with tides (Fig. S3 (c)), Blake exhibits uplift twice in a single high-tide to low-tide transition (Fig. S4 (c)). Uplift landwards of G during low-tide would be consistent with existence of a fulcrum

at G leveraging vertical displacement that is in anti-phase with tides. However, because the detected vertical deflection is at the cm-limit and differs between different processing schemes, it is difficult to judge from the GNSS data alone if this signal is significant. As we will now show, the TRI data solidify this finding.

The TRI time series of differential interferograms with $\Delta t = 12$ h show unaliased tidal signatures in the majority of the cases with much spatial and temporal detail (Fig. 4). Gaps in the time series are due to temporal decorrelation and can be mitigated by choosing smaller Δt. The differential TRI and the differential GNSS data can be compared using the previously defined projection between both reference systems. For Tuati and Blake, this results in a good fit between GNSS and TRI data at the cm-level (Fig. 2e-h). The fit is better for PPP processing than for D-GNSS, although both processing types differ little in their timing and shape of vertical and horizontal displacements (Supplementary Information 2). This shows that cm-scale differences are fully represented in the differential TRI data, and that TRI can here be used to validate GNSS. In particular, neglecting the double uplift pattern at Blake results in a worse fit to the TRI data rendering this signal meaningful.

Unlike GNSS, the differential TRI data show regular tidal patterns more than 6 km upstream of G. At peak tidal displacement, the time series shows two zones of differing polarity (Fig. 4a,b). Seawards of the hinge line, differential vertical displacement of the ice shelf is dominant. The differential horizontal components at this location are of equal magnitude, but cancel due to our specific viewing geometry (Fig. 2e-h). Landwards of the hinge line, the TRI observes a mixed signal of horizontal and vertical components. This results in a shift of the differential LOS displacement that follows the ice-shelf signatures with an approx. 6 h time lag. The fact that horizontal components typically do not cancel during the interferogram differencing makes the delineation of the grounding zone in individual interferograms more delicate, particularly with respect to inferring grounding-line migration rates. However, in our case the complete time series over multiple tidal cycles is consistent, and suggests that the grounding line migrates very little, if at all, over these timescales.

3.4 Discussion and Conclusion

The TRI data delivers a spatio-temporal time series of an ice stream that is consistent with 6 hourly GNSS observations at the grounding line (i.e., at Tuati) and 2 km further upstream on grounded ice (i.e., Blake). Even further upstream (i.e., Hillary) tidal frequencies still occur in the TRI data but cannot be resolved anymore with GNSS. This shows that TRI detects horizontal and vertical components of ice-stream dynamics on tidal timescales and at cm-resolution, even in areas where the viewing geometry is not favourable to some of these components. The PCA quantifies the upstream extent ($>$ 10 km) of diurnal tidal signatures in the ice-stream dynamics. These decay near-linearly with distance and are almost synchronous to the corresponding tidal forcing. Spatial patterns show across-flow variability where tidal signatures propagate more strongly on the ice stream's true right side (Fig. 3c). The asymmetry is matched by the geometry of constraining mountain ranges. This is consistent with decoupling from the true right shear zone and enables a longer transmission of tidal stresses (Thompson et al., 2014). Moreover, the flowfield time series follows the diurnal tidal forcing and has no semi-diurnal component. It is therefore unlikely that previously suggested flexural softening through tidal bending on the ice shelf (which would lead to frequency doubling in ice-stream dynamics (Rosier & Gudmundsson, 2018)) is a relevant process at Priestley Glacier.

There are several implications from the analysis of the tidal flexure patterns. First, the observed double uplift at Blake is significant as it matches the TRI observations. Such a pattern has been reported previously only at Ekstrm Ice Shelf (Heinert & Riedel, 2007). The first uplift during high-tide can be explained by uplift of the adjacent ice shelf as

Blake is close to H. The second uplift during low-tide can be explained by ephemeral regrounding during low-tide, resulting in an ephemeral fulcrum. Because we do not observe significant grounding-line migration, the regrounding must occur close to the grounding-line location at high-tide. The existence of a fulcrum is important, given that even small surface deflections have a significant impact on the subglacial hydrology (Walker et al., 2013), basal properties, and grounding zone stability (Christianson et al., 2013). Second, horizontal velocities vary significantly over tidal cycles and do not cancel during double differencing. An example for this is our own analysis of the Sentinel 1A data, where the inferred variability of the hinge zone over several years (Fig. S7) may rather reflect unresolved differences in horizontal flow than a grounding-line migration pattern which is not observed in the TRI dataset. Satellite acquisitions also rarely sample the tidal extremes and most triple difference capture intermediate stages of tidal flexure. In such time series, it is difficult to distinguish whether hinge line migration is induced by tides or by long-term grounding line migration. TRI does not have these limitations.

Third, the differential tidal signatures in ice flow can be observed more than 6 km upstream of the grounding line even though the tidal amplitudes of ± 0.4 m are comparatively small. The differential ice-flow patterns show no significant phase shift with increasing distance from the grounding line suggesting that the underlying process is communicated instantaneously. Some of the variability may hence be explained with ice elasticity, where vertical deflections are accompanied by horizontal shortening/extension at the surface(Rack et al., 2017). Other explanations (i.e., communication via changes in the subglacial hydrological system) may also be involved, but must comply with the observed signatures in the TRI data.

The largest drawback of TRI interpretation is the projection into LOS which makes the recovered flow field in parts non intuitive. This is resolvable locally with concurrent GNSS observations, or area-wide, by using two or more TRIs (Voytenko et al., 2017). However, the projection from a 3D reference frame into LOS is purely geometric and contains no tuning factors. This means that both the time series of LOS flowfields and the LOS flexure patterns are a new observational benchmark that can be used to test ice-flow models in order to isolate the dominating processes of ice-stream mechanics.

Acknowledgments
Drews was supported by an Emmy Noether Grant of the Deutsche Forschungsgemeinschaft(DR 822/3-1). Wild, Marsh and Rack were supported by a NZ Antarctic Research Institute Type-A Grant 2018-1. Neckel was supported by EU's Horizon 2020 research and innovation programme (grant No 689443). We would like to thank Antarctica New Zealand and the Korea Polar Research Institute for logistical support on the Priestley Glacier. We thank H. Han and J. Lee for fruitful discussions relating to field work. Field work was made possible with support of R. Bottomly and J. Southward. We acknowledge Heimplanet Entwicklungs GmBH for provision of a dome tent to house the TRI. Ice-penetrating radar data used in this study were acquired by NASAs Operation IceBridge.

For the time of review, data are available at:

https://esdynamics.geo.uni-tuebingen.de/nextcloud/index.php/s/S3imaDRqtYCjmR4

A request to upload the data to the Pangaea long-term storage archive is currently being processed.

References

Caduff, R., Schlunegger, F., Kos, A., & Wiesmann, A. (2015). A review of terrestrial radar interferometry for measuring surface change in the geosciences. *Earth*

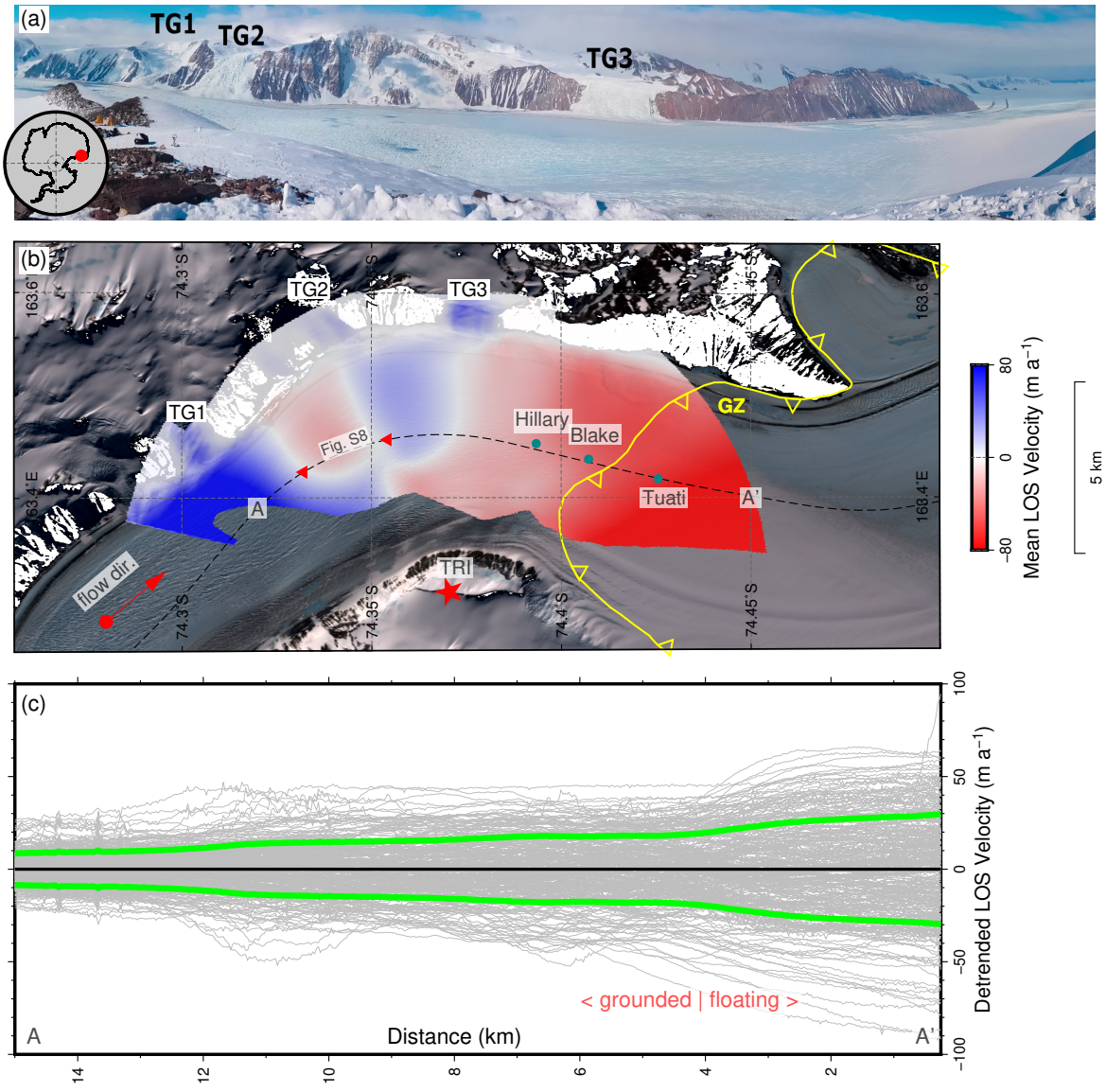

Figure 1. (a) Panoramic view from TRI location overlooking Priestley Glacier with three marked tributary glaciers (TG 1-3). Ice flow direction is from left (north) to right (south). (b) Mean ice flow in the line-of-sight (LOS) direction with positive values marking ice movement towards the TRI. Hillary, Blake and Tuati are GNSS stations. Red triangles mark Bull's eye location referred to in the main text. The estimated landward limit of the grounding zone (GZ) is shown with a yellow curve. Background image is acquired by Sentinel 2. (c) Deviation from the mean of ice flow along A-A' over an 8 day period. Gray curves are taken approximately every 0.5 hours and each curve represents a temporal average over 3h. Green curves mark ± one standard deviation.

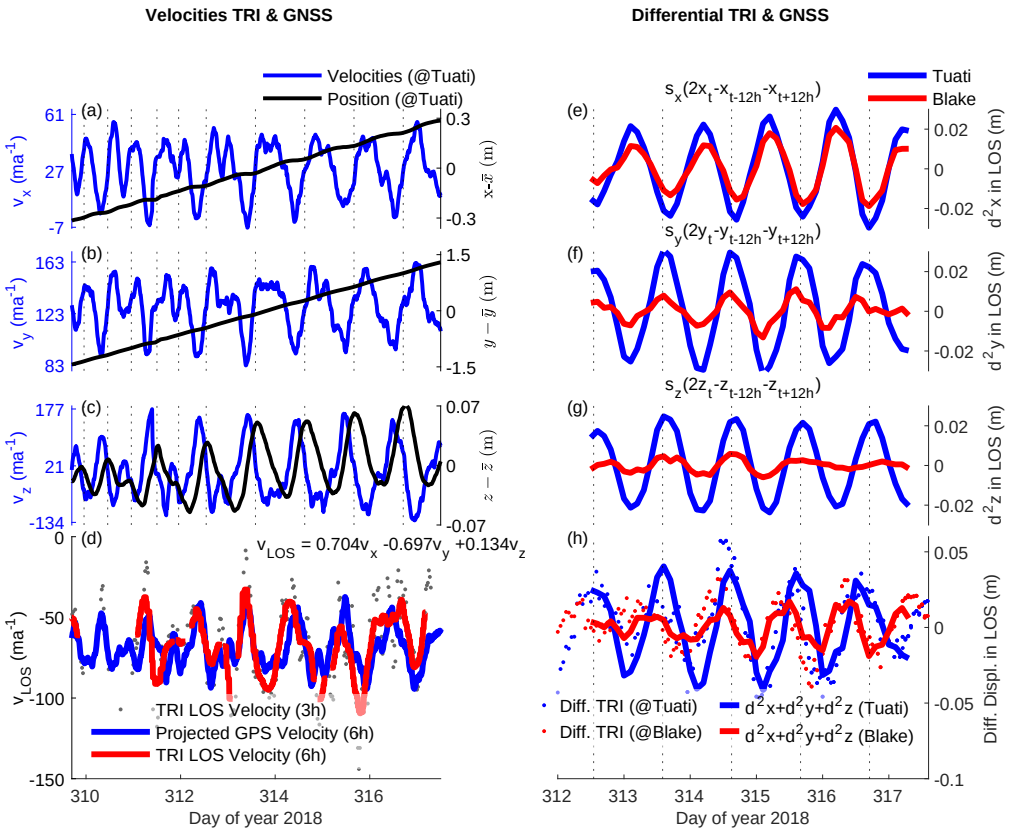

Figure 2. Time series over 8 days of of horizontal **(a, b)** and vertical **(c)** ice flow measured at GNSS station Tuati. Projection into line-of-sight geometry demonstrates good fit between TRI and GNSS velocities **(d)**. Velocity differences over 12h intervals (i.e., the time difference between high-tide and low-tide) at GNSS stations Tuati and Blake are evident in line-of-sight both in the differential horizontal **(e,f)** and differential vertical displacement **(g)**. The sum of these components results in a fit to the differential TRI signal at the cm-level **(h)**. Gray dashed vertical lines in all panels mark times of high-tide for reference (Padman et al., 2002).

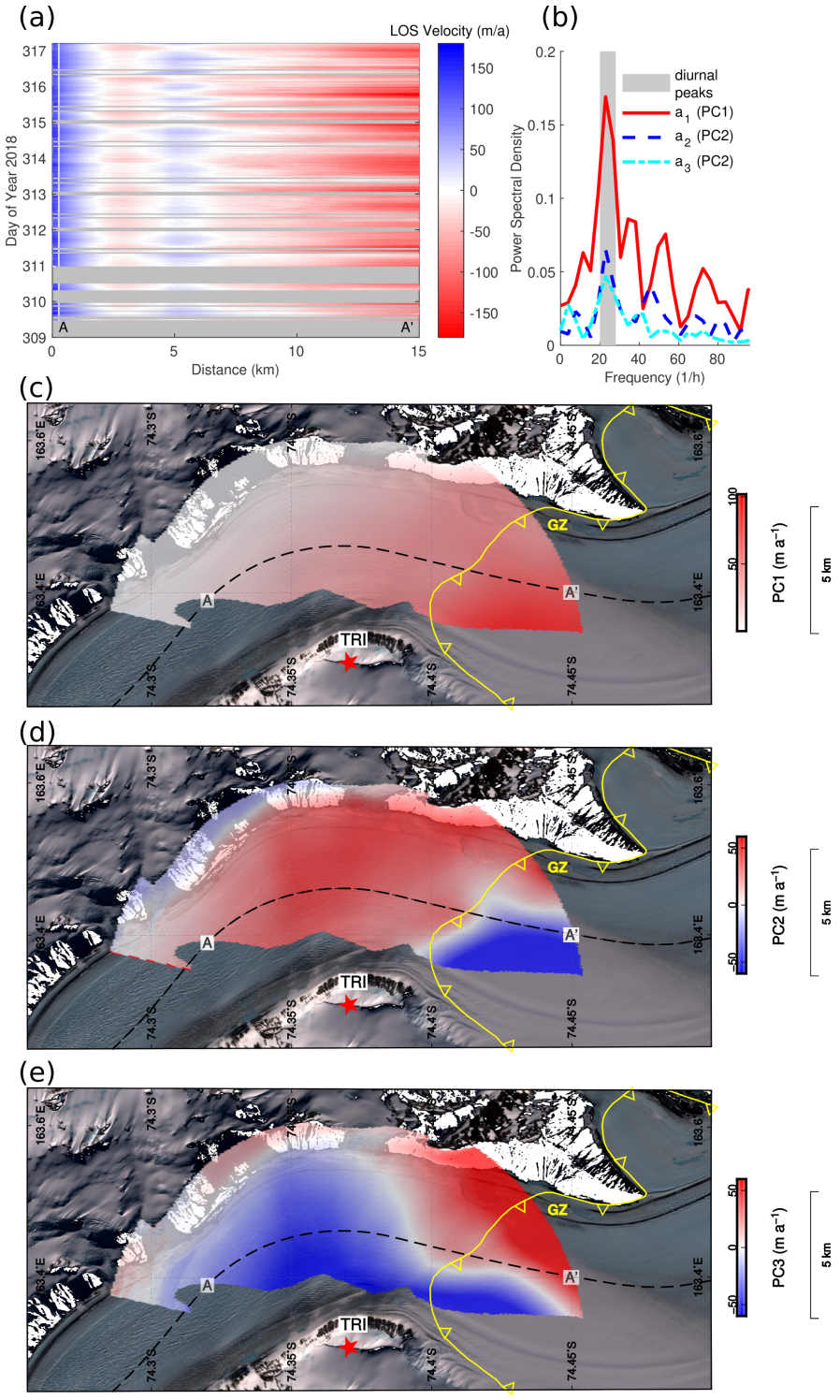

Figure 3. (a) Time series along profile A-A' of 3-hourly averaged flowfields in LOS. (b) Spectrum of the scores a_1, a_2, and a_3 signifying the temporal variability of principal component 1, 2, and 3 shown in (d)-(f), respectively. The total variance explained by the first three principal components is 85% (=65% (PC1) + 13% (PC2)+ 7 (PC3)%). The estimated landward limit of the grounding zone (GZ) is shown with a yellow curve.

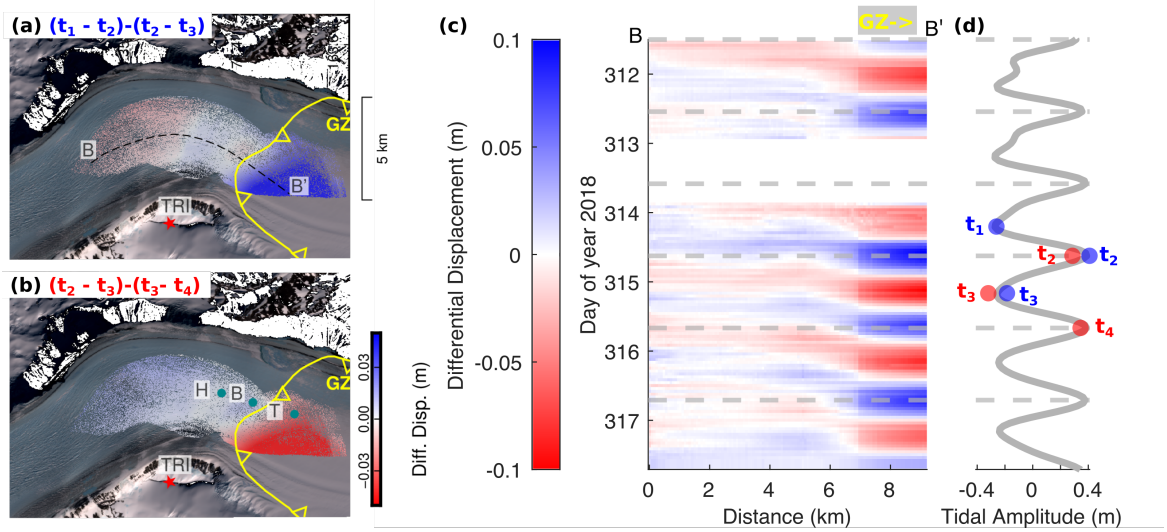

Figure 4. Differential displacement fields for image triplets covering a low-tide to low-tide **(a)** and a high-tide to high-tide **(b)** cycle. The landward limit of the grounding zone (GZ) is marked with a yellow curve. The full differential time series along transect B-B' (located in (a)) is shown in **(c)** in relation to the predicted tidal amplitudes (Padman et al., 2002) **(d)**.

Surface Processes and Landforms, *40*(2), 208–228. doi: 10.1002/esp.3656

Campbell, A. J., Hulbe, C. L., & Lee, C.-K. (2017). The shape of change: an EOF approach to identifying sources of transient thickness change in an ice shelf. *Annals of Glaciology*, *58*(74), 21–27. doi: 10.1017/aog.2017.16

Christianson, K., Parizek, B. R., Alley, R. B., Horgan, H. J., Jacobel, R. W., Anandakrishnan, S., ... Muto, A. (2013). Ice sheet grounding zone stabilization due to till compaction. *Geophysical Research Letters*, *40*(20), 5406–5411. doi: 10.1002/2013GL057447

Fricker, H. A., Coleman, R., Padman, L., Scambos, T. A., Bohlander, J., & Brunt, K. M. (2009). Mapping the grounding zone of the Amery Ice Shelf, East Antarctica using InSAR, MODIS and ICESat. *Antarctic Science*, *21*(05), 515. doi: 10.1017/S095410200999023X

Gudmundsson, G. H. (2006). Fortnightly variations in the flow velocity of Rutford Ice Stream, West Antarctica. *Nature*, *444*(7122), 1063–1064. doi: 10.1038/nature05430

Heinert, M., & Riedel, B. (2007). Parametric modelling of the geometrical ice-ocean interaction in the Ekstroemisen grounding zone based on short time-series. *Geophysical Journal International*, *169*(2), 407–420. doi: 10.1111/j.1365-246X.2007.03364.x

Howat, I. M., Porter, C., Smith, B. E., Noh, M.-J., & Morin, P. (2019). The Reference Elevation Model of Antarctica. *The Cryosphere*, *13*(2), 665–674. doi: 10.5194/tc-13-665-2019

Joughin, I. R., Winebrenner, D. P., & Fahnestock, M. A. (1995). Observations of ice-sheet motion in Greenland using satellite radar interferometry. *Geophysical Research Letters*, *22*(5), 571–574. doi: 10.1029/95GL00264

Marsh, O. J., Rack, W., Floricioiu, D., Golledge, N. R., & Lawson, W. (2013). Tidally induced velocity variations of the Beardmore Glacier, Antarctica, and their representation in satellite measurements of ice velocity. *The Cryosphere*, *7*(5), 1375–1384. doi: 10.5194/tc-7-1375-2013

Minchew, B. M., Simons, M., Riel, B., & Milillo, P. (2017). Tidally induced vari-

ations in vertical and horizontal motion on Rutford Ice Stream, West Antarctica, inferred from remotely sensed observations. *Journal of Geophysical Research: Earth Surface*, *122*(1), 167–190. doi: 10.1002/2016JF003971

Paden, J., Li, J., Rodriguez-Morales, F., & Hale, R. (2010). IceBridge MCoRDS L2 Ice Thickness, Version 1. Boulder, Colorado USA. NASA National Snow and Ice Data Center Distributed Active Archive Center. doi: https://doi.org/10.5067/GDQ0CUCVTE2Q

Padman, L., Fricker, H. A., Coleman, R., Howard, S., & Erofeeva, L. (2002). A new tide model for the Antarctic ice shelves and seas. *Annals of Glaciology*, *34*, 247–254. doi: 10.3189/172756402781817752

Padman, L., Siegfried, M. R., & Fricker, H. A. (2018). Ocean Tide Influences on the Antarctic and Greenland Ice Sheets: Tide Influences on Ice Sheets. *Reviews of Geophysics*, *56*(1), 142–184. doi: 10.1002/2016RG000546

Rack, W., King, M. A., Marsh, O. J., Wild, C. T., & Floricioiu, D. (2017). Analysis of ice shelf flexure and its InSAR representation in the grounding zone of the southern McMurdo Ice Shelf. *The Cryosphere*, *11*(6), 2481–2490. doi: 10.5194/tc-11-2481-2017

Riedel, B., Nixdorf, U., Heinert, M., Eckstaller, A., & Mayer, C. (1999). The response of the Ekstrmisen (Antarctica) grounding zone to tidal forcing. *Annals of Glaciology*, *29*, 239–242. doi: 10.3189/172756499781821247

Rignot, E. (1996). Tidal motion, ice velocity and melt rate of Petermann Gletscher, Greenland, measured from radar interferometry. , *42*(142), 476–485. doi: 10.1017/S0022143000003464

Rignot, E., Mouginot, J., & Scheuchl, B. (2011). Ice flow of the Antarctic ice sheet. *Science*, *333*(6048), 1427–1430. doi: 10.1126/science.1208336

Rosen, P. A., Hensley, S., Joughin, I. R., Li, F., Madsen, S. N., Rodriguez, E., & Goldstein, R. M. (2000). Synthetic Aperture Radar Interferometry. , *88*(3).

Rosier, S. H. R., & Gudmundsson, G. H. (2016). Tidal controls on the flow of ice streams:. *Geophysical Research Letters*, *43*(9), 4433–4440. doi: 10.1002/2016GL068220

Rosier, S. H. R., & Gudmundsson, G. H. (2018). Tidal bending of ice shelves as a mechanism for large-scale temporal variations in ice flow. *The Cryosphere*, *12*(5), 1699–1713. doi: 10.5194/tc-12-1699-2018

Rosier, S. H. R., Gudmundsson, G. H., & Green, J. A. M. (2015). Temporal variations in the flow of a large Antarctic ice stream controlled by tidally induced changes in the subglacial water system. *The Cryosphere*, *9*(4), 1649–1661. doi: 10.5194/tc-9-1649-2015

Rosier, S. H. R., Gudmundsson, G. H., King, M. A., Nicholls, K. W., Makinson, K., & Corr, H. F. J. (2017). Strong tidal variations in ice ow observed across the entire Ronne Ice Shelf and adjoining ice streams. , 12.

Scott, J. B. T., Gudmundsson, G. H., Smith, A. M., Bingham, R. G., Pritchard, H. D., & Vaughan, D. G. (2009). Increased rate of acceleration on Pine Island Glacier strongly coupled to changes in gravitational driving stress. *The Cryosphere*, 7.

Smith, A. (1991). The use of tiltmeters to study the dynamics of Antarctic ice-shelf grounding lines. *Journal of Glaciology*, *37*(125), 51–58. doi: 10.3189/S0022143000042799

Thompson, J., Simons, M., & Tsai, V. C. (2014). Modeling the elastic transmission of tidal stresses to great distances inland in channelized ice streams. *The Cryosphere*, *8*(6), 2007–2029. doi: 10.5194/tc-8-2007-2014

Voytenko, D., Dixon, T. H., Holland, D. M., Cassotto, R., Howat, I. M., Fahnestock, M. A., ... De La Pea, S. (2017). Acquisition of a 3 min, two-dimensional glacier velocity field with terrestrial radar interferometry. *Journal of Glaciology*, *63*(240), 629–636. doi: 10.1017/jog.2017.28

Voytenko, D., Stern, A., Holland, D. M., Dixon, T. H., Christianson, K., & Walker, R. T. (2015). Tidally driven ice speed variation at Helheim Glacier, Greenland, observed with terrestrial radar interferometry. *Journal of Glaciology*, *61*(226), 301–308. doi: 10.3189/2015JoG14J173

Walker, R. T., Parizek, B. R., Alley, R. B., Anandakrishnan, S., Riverman, K. L., & Christianson, K. (2013). Ice-shelf tidal flexure and subglacial pressure variations. *Earth and Planetary Science Letters*, *361*, 422–428. doi: 10.1016/j.epsl.2012.11.008

Wild, C. T., Marsh, O. J., & Rack, W. (2019). Differential interferometric synthetic aperture radar for tide modelling in Antarctic ice-shelf grounding zones. *The Cryosphere*, *13*(12), 3171–3191. doi: 10.5194/tc-13-3171-2019

Xie, S., Dixon, T. H., Voytenko, D., Deng, F., & Holland, D. M. (2018). Grounding line migration through the calving season at Jakobshavn Isbr, Greenland, observed with terrestrial radar interferometry. *The Cryosphere*, *12*(4), 1387–1400. doi: 10.5194/tc-12-1387-2018

Figure 1.

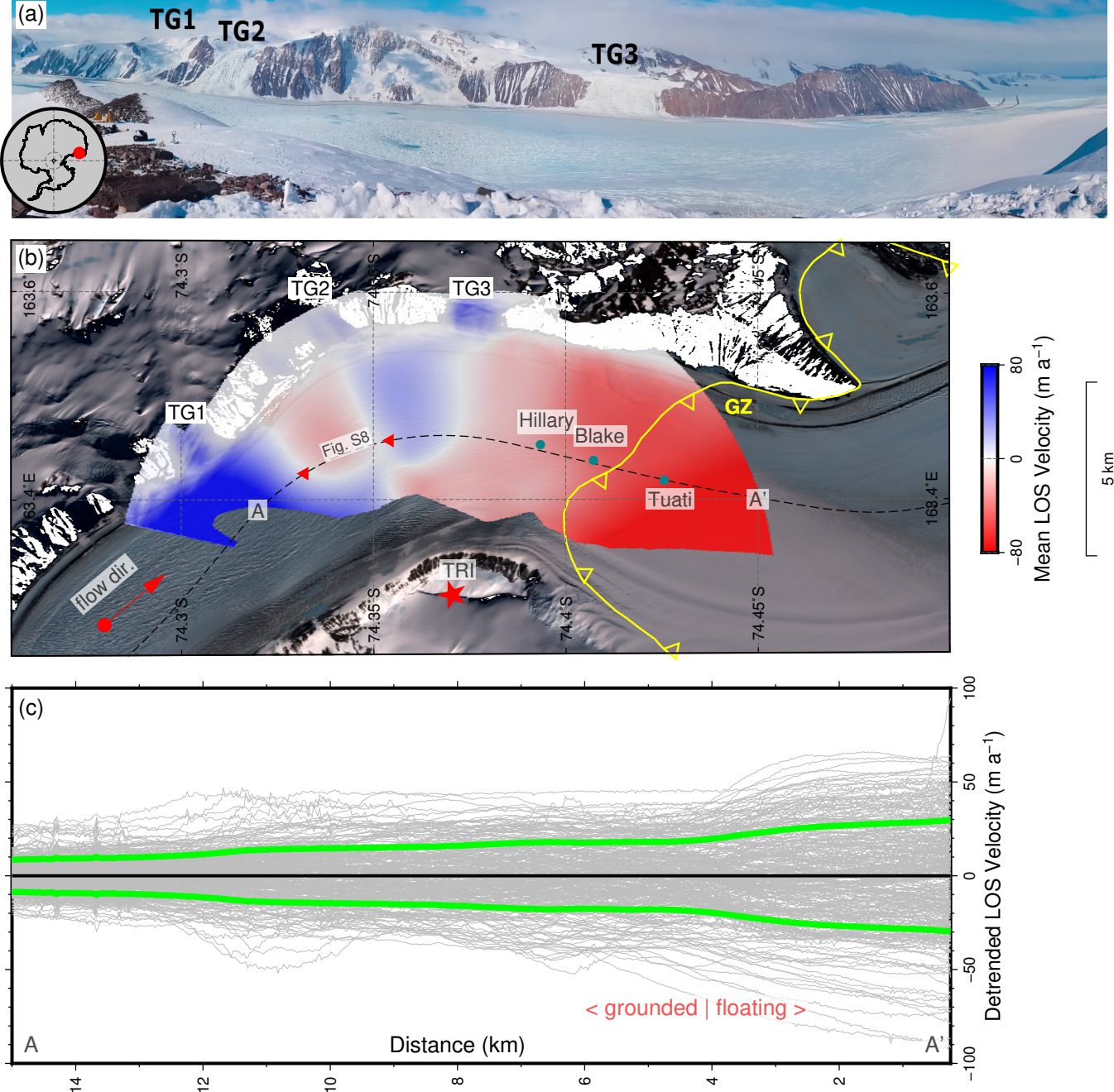
(a)
TG1
TG2
TG3
(b)
TG1
TG2
TG3
GZ
Hillary
Blake
Tuati
A
A'
Fig. S8
TRI
flow dir.
163.6°
74.3°S
74.35°S
74.4°S
74.45°S
168.4°E
5 km
Mean LOS Velocity (m a⁻¹)
80
0
−80
(c)
< grounded | floating >
A
Distance (km)
A'
Detrended LOS Velocity (m a⁻¹)
100
50
0
−50
−100
14
12
10
8
6
4
2

Figure 2.

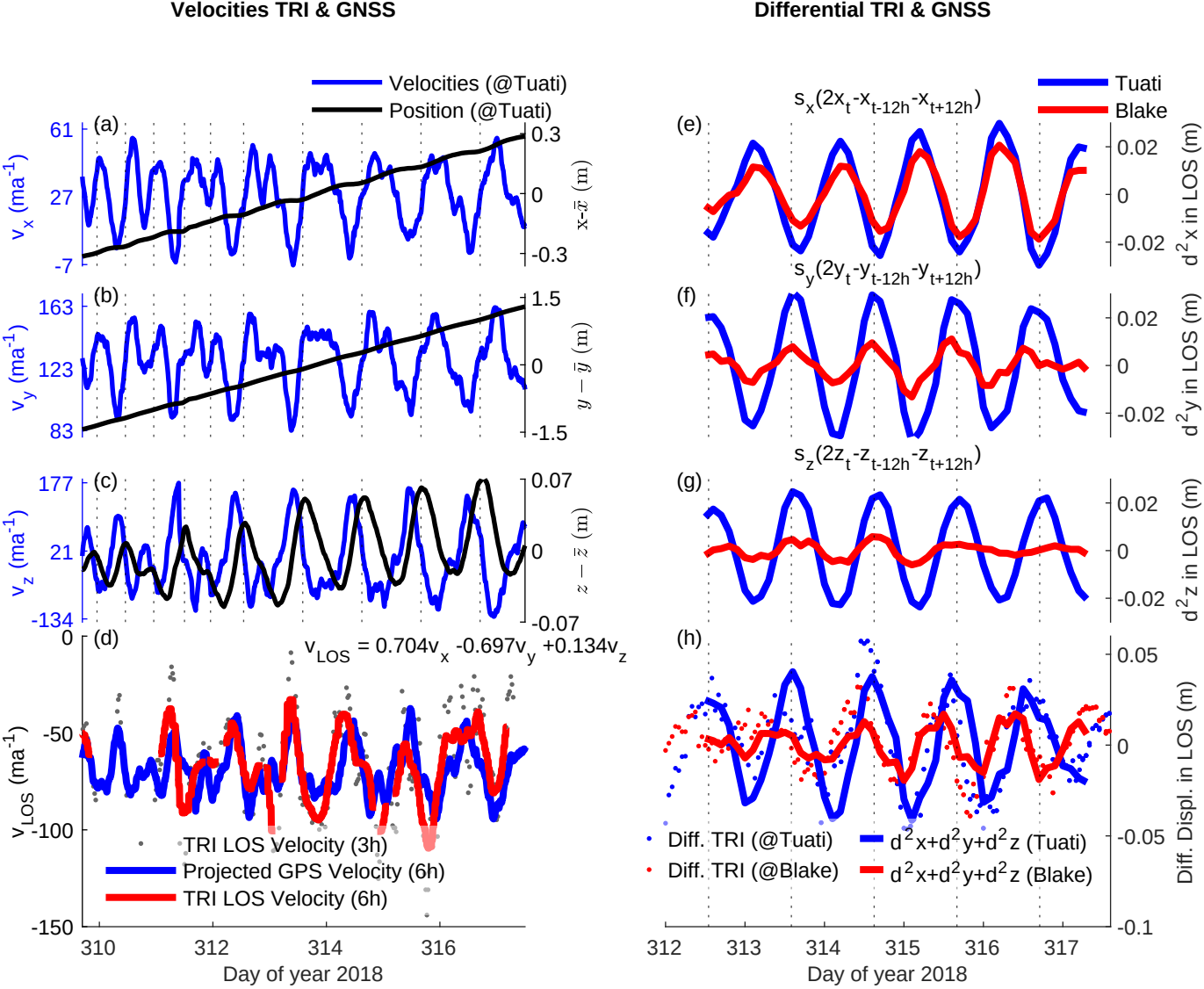
Velocities TRI & GNSS
Differential TRI & GNSS
Velocities (@Tuati)
Position (@Tuati)
(a)
(b)
(c)
(d)
(e)
(f)
(g)
(h)
v_x (ma^{-1})
v_y (ma^{-1})
v_z (ma^{-1})
$x-\bar{x}$ (m)
$y-\bar{y}$ (m)
$z-\bar{z}$ (m)
$v_{LOS} = 0.704v_x - 0.697v_y + 0.134v_z$
v_{LOS} (ma^{-1})
TRI LOS Velocity (3h)
Projected GPS Velocity (6h)
TRI LOS Velocity (6h)
Day of year 2018
$s_x(2x_t - x_{t-12h} - x_{t+12h})$
$s_y(2y_t - y_{t-12h} - y_{t+12h})$
$s_z(2z_t - z_{t-12h} - z_{t+12h})$
Tuati
Blake
d^2x in LOS (m)
d^2y in LOS (m)
d^2z in LOS (m)
Diff. TRI (@Tuati)
Diff. TRI (@Blake)
$d^2x+d^2y+d^2z$ (Tuati)
$d^2x+d^2y+d^2z$ (Blake)
Diff. Displ. in LOS (m)
Day of year 2018

Figure 3.

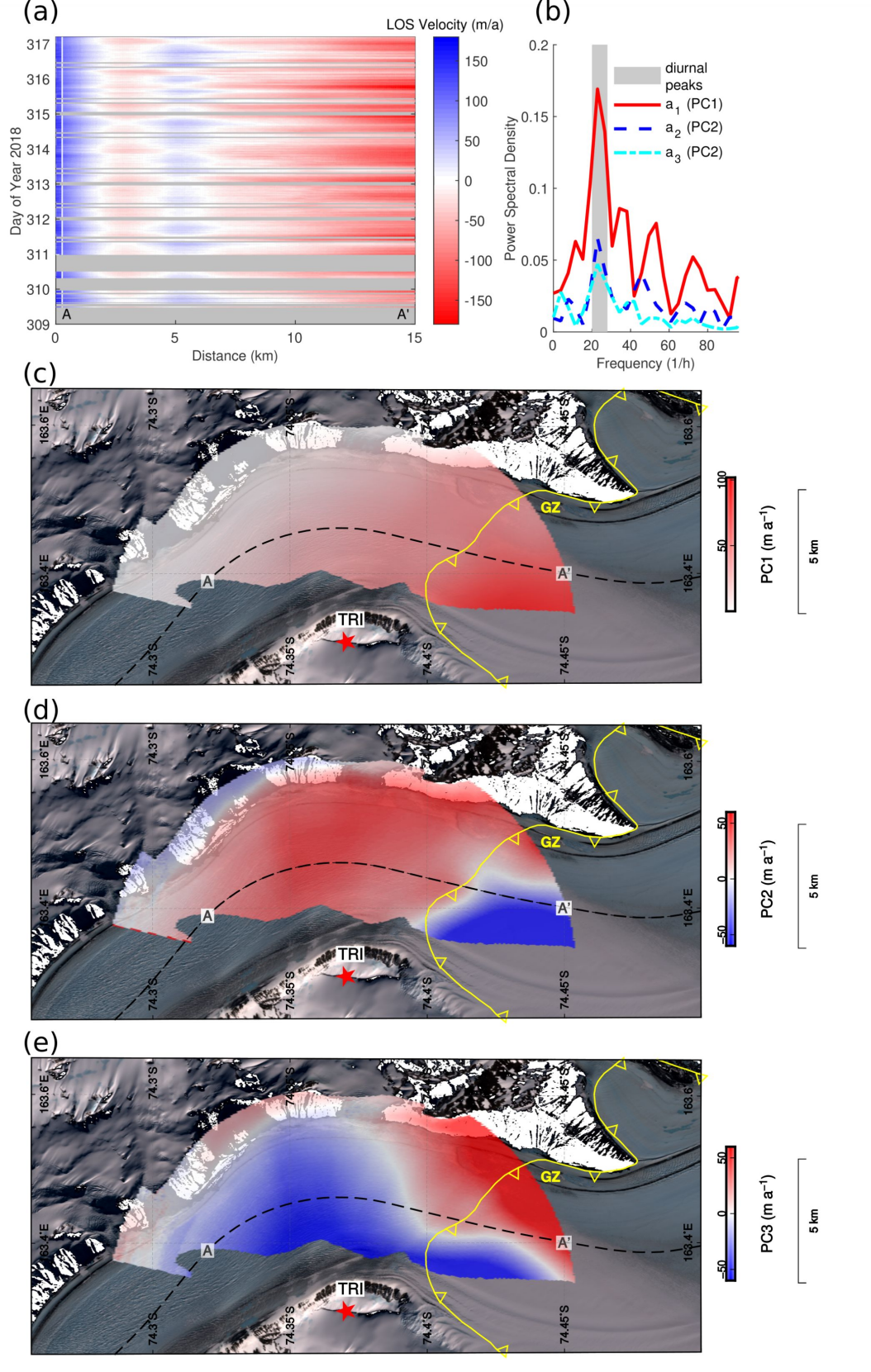
(a)
LOS Velocity (m/a)
Day of Year 2018
Distance (km)
A
A'
(b)
diurnal peaks
a1 (PC1)
a2 (PC2)
a3 (PC2)
Power Spectral Density
Frequency (1/h)
(c)
GZ
TRI
PC1 (m a−1)
5 km
(d)
PC2 (m a−1)
(e)
PC3 (m a−1)

Figure 4.

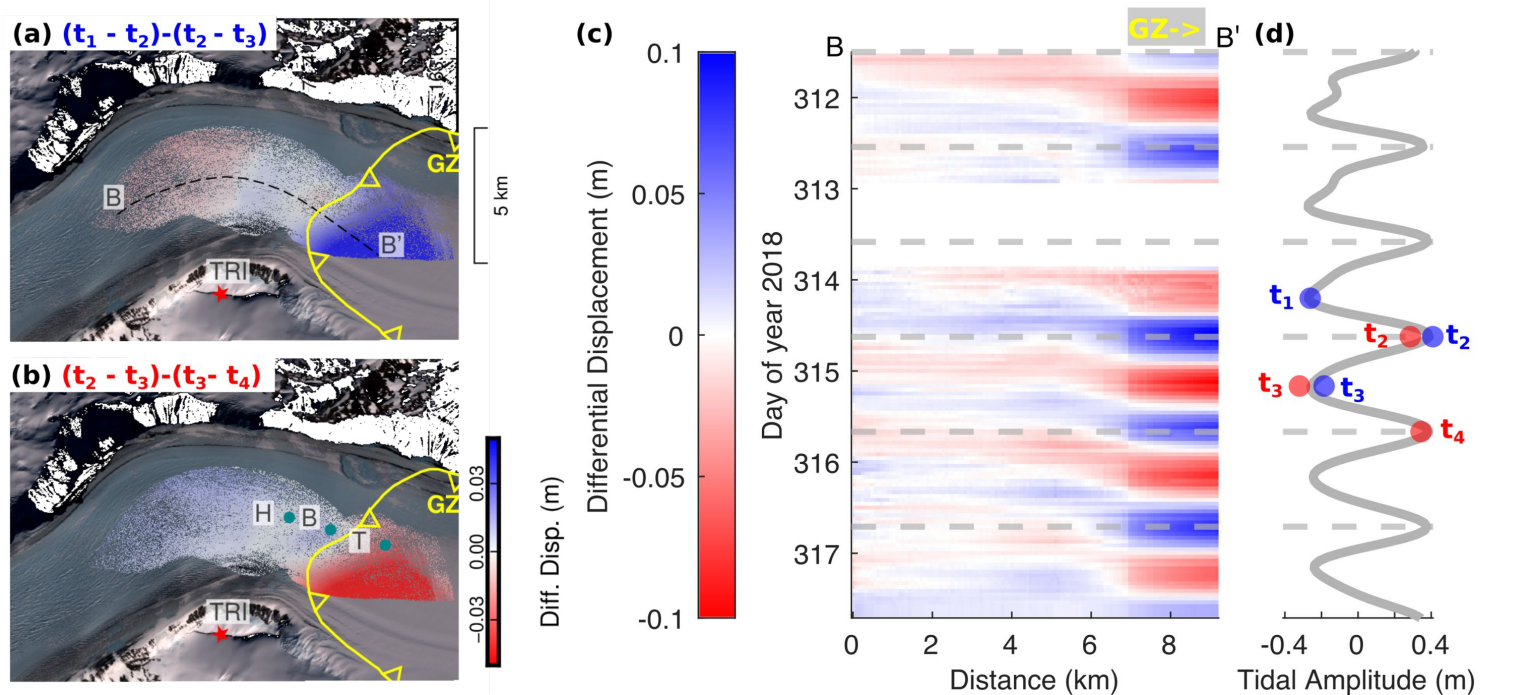
(a) (t1 - t2)-(t2 - t3)
B
B'
GZ
TRI
5 km
(b) (t2 - t3)-(t3- t4)
H
B
T
GZ
TRI
0.03
0.00
−0.03
Diff. Disp. (m)
(c)
0.1
0.05
0
-0.05
-0.1
Differential Displacement (m)
B
B'
GZ->
312
313
314
315
316
317
Day of year 2018
0
2
4
6
8
Distance (km)
(d)
t1
t2
t2
t3
t3
t4
-0.4
0
0.4
Tidal Amplitude (m)